

Freeform wide-angle camera lens enabling mitigable distortion

ZHENFENG ZHUANG,^{1,*} JOCELYN PARENT,¹ PATRICE ROULET,¹ AND SIMON THIBAUT^{1,2}

¹Immersion Inc, 2020 Robert-Bourassa Blvd., Suite 2320, Montreal, Quebec, H2A 2A5, Canada

²Centre d'optique, photonique et laser, Département de physique, de génie physique et d'optique, Université Laval, 2375, rue de la Terrasse, Québec G1V 0A6, Canada

*Corresponding author: zhenfeng.zhuang@immersion.com

Received 11 February 2022; revised 18 May 2022; accepted 26 May 2022; posted 2 June 2022; published 16 June 2022

Allowing natural scenes as well as maximizing field of view (FoV) can benefit from the minimization of distortion for the wide-angle camera. The wide-angle camera utilizing freeform surfaces for mitigating distortions, either barrel distortion or pincushion distortion, is therefore of interest. In this paper, the designs of using all-aspherical surfaces and aspherical surfaces combined with freeform surfaces are investigated. To minimize the deviation before and after converting from aspherical surfaces to freeform surfaces, a mathematical conversion scheme is derived. By applying it to the design example, the methodology is shown to be effective in the case of an optical system with a large number of aspherical/freeform surfaces. Additionally, custom freeform analysis tools are developed for quantitative analysis and visualization of the critical characteristics of optical performance, namely, a 2D lateral color field map, 2D relative illumination field map, 2D spot radius field map, and 2D average modulation transfer function (MTF) field map. Compared to classical all-aspherical design, simulation results show that freeform design has the capability to reduce distortion, and other performances such as relative illumination, spot size, and MTF can also be improved, even though there are some compromises on the peripheral FoV. The design approach will have potential important research and application values for lens systems utilized in miniature camera lenses, especially the wide FoV capability. © 2022 Optica Publishing Group

<https://doi.org/10.1364/AO.456127>

1. INTRODUCTION

A wide-angle camera lens is the most prominent component for myriad applications ranging from civilian use to military use, from surveillance to entertainment, and from medical imaging applications to engineering applications. Wide-angle camera lenses yield a larger field of view (FoV), but they also introduce undesirable effects owing to lens optics, such as non-uniform illumination and distortion. These distortions can stretch, squish, or skew objects and make them difficult to recognize or to look unnatural to observers. Therefore, a wide-angle camera with little or no distortion is preferred by users with the emergence of technologies and applications.

One of the most prevalent methods of lens distortion correction is using image processing [1–3], since one of the main functions is to accurately correct the distortion in a wide-angle camera system. However, the distortion should be interpreted as accurate as possible through the calibration procedure, aiming to avoid huge deviation between measurement results and real results. In addition, the camera parameters have notable influence on the results of the calibration process. A real-time implementation of distortion correction presents several problems and constraints [4]. Limitations arise in the case of image

processing. Therefore, designing a wide-angle lens with less distortion or no distortion is more straightforward.

A wide FoV with a compact structure for the capsule endoscope application was proposed [5]. However, because of the wide FoV, the television (TV) distortion, which was -28% , was difficult to correct, since even aspheric surfaces were implemented. A dual view capsule endoscopic lens was introduced [6], and due to the characteristics of the configuration, the FoV for the front view was able to reach 90° , while the FoV for the back view was 260° – 290° . The distortion was considerably large. Combining with freeform optics, methods such as the use of partial differential equations [7] or simultaneous multiple surfaces [8,9] enable the initial surface to be obtained, and then optimization was further carried out to improve image quality. Using these methods, a wide-angle lens with low distortion can be obtained [10–12]. Miniature camera lenses can be both lightweight and compact, using one or two S-shaped aspheric elements that have different curvature directions from the center of the surface to the peripheral surface to act as a field flattener so that a flat sensor can be utilized. A pedal surface polynomial to model an S-shaped surface in miniature camera lenses was introduced [13–15]. The pedal freeform lens shows better nominal optical performance across the full field. However, a

least-squares fitting algorithm should be implemented to eliminate the deviation between an aspheric surface and pedal-based freeform surface. The overall optical system was set to be symmetrical with respect to the optical axis. Nevertheless, distortion was inevitable.

The theory and development of freeform optics in imaging applications have been reported in the literature [16]. However, reports of the expense of miniature camera lenses using freeform optics are scarce. In this paper, we introduce a considerable improvement in image performance in wide-angle lenses where the S-shaped surfaces are modeled as freeform surfaces. To the best of our knowledge, this is the first time introducing the mathematical conversion scheme between aspheric and freeform surfaces without sacrificing optical performance. Aspheric surfaces in conjunction with freeform surfaces are utilized to realize a low-distortion characteristic. The reasons for selecting the desired freeform surface description, design approach, and strategy of a freeform wide-angle camera lens are detailed. The design procedures of the starting point, all-aspherical design, as well as freeform design are demonstrated. Analysis tools using the field map feature are developed to visualize performances for non-symmetrical systems. We envision that the research content presented in this paper may inspire researchers to pursue other analysis tools for non-symmetrical optical systems. Moreover, we elaborate the penalty of using freeform surfaces compared to traditional all-aspherical design, which has never been discussed in the literature. The study of the allowance of freeform surfaces could provide some references for other freeform techniques.

2. DESIGN METHODOLOGY

A. Choice of Freeform Surface Type

Freeform optics is becoming more mature because of improvements in manufacturing processes and functionalities. The earliest launching point of freeform optics in imaging optics was anamorphic optics, which combined spherical, aspherical, and toroidal surfaces. However, the toroidal surface cannot offer higher degrees of freedom for imaging system design due to the different contributions of optical power along orthogonal axes. With the rapid development of optical metrology technologies for freeform optics, it naturally gives rise to a new definition of freeform optics. Mathematically, freeform surfaces can be categorized as orthogonal polynomials such as Zernike polynomials and Q -polynomials, and non-orthogonal functions such as xy polynomials, radial basis functions, and non-uniform rational B-splines (NURBS) [16,17]. However, most manufactures are unable to fabricate such types of lenses due to the uncommon surface description. Examples for such complex freeform surface descriptions include: Q -type aspheric, spline surface, φ -polynomial surface, radial basis functions, and NURBS. They must convert to a standard representation to reduce surface complexity and maintain performance. However, the degradation of optical performances is inevitable because of the inaccuracy of the fitting algorithm. Thus, it is very important to select a suitable freeform method for freeform surface representation. Historically, Zernike and xy polynomials have certainly been the most extensively used for characterizing optical freeform surfaces in a variety of applications. A critical

aspect of Zernike terms is that they demonstrate a direct connection to optical aberrations; thus, Zernike polynomials are widely adopted in optical fabrication and testing. With the rapid developments in manufacturing freeform surfaces as well as in freeform optics metrology to accurately measure freeform optics, the xy polynomial, which affords abundant degrees of freedom and has the capability of aberration correction, is an appealing solution to represent freeform surfaces in a standard format.

B. Utilization of Freeform Surface

The design process of the freeform-based wide-angle camera lens mainly consists of the following six steps.

- (1) Assessment of the design specifications, including total track length (TTL), FoV, f -number, relative illumination (RI), lateral color, and distortion.
- (2) Determination of the starting point in accordance with the design requirement.
- (3) Optimization of the rotationally symmetrical system. In the initial stage, as illustrated in Fig. 1(a), the half-FoV has to be sampled and optimized in the radial direction in a rotationally symmetric optical system. It is important to make the performance meet the design demand as much as possible at this stage.
- (4) Due to the symmetry about the XOZ and YOZ planes, a quarter of the full FoV should be sampled in a rectangular grid. Figure 1(b) demonstrates the field sampling strategy during this stage of optimization. Most distortion-free optical systems are described by f -tan(θ) distortion. The mapping between object space and image space can be built and given as follows:

$$\begin{cases} x' = f_x \tan(\theta_x), \\ y' = f_y \tan(\theta_y), \end{cases} \quad (1)$$

where f_x and f_y represent the effective focal length in the XOZ and YOZ planes, respectively; the FoV and corresponding image height can be described as (θ_x, θ_y) and (x', y') , respectively.

- (5) After the first step of optimization, an optimal surface is selected and converts the surface type to an xy -polynomial surface from an aspheric surface for further optimization, aiming to obtain a distortion-free wide-angle camera lens. The sag z of the xy -polynomial freeform surface is mathematically represented by

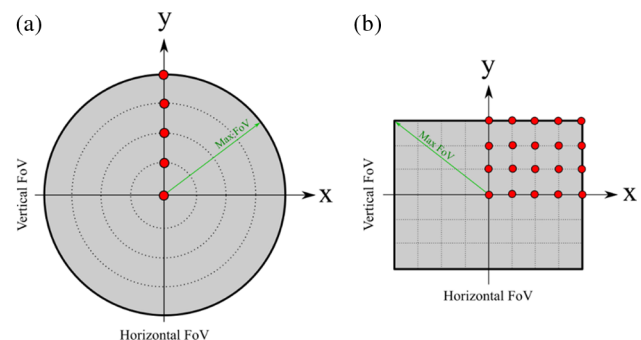


Fig. 1. (a) Sampled fields in the radial direction in a rotationally symmetric system; (b) sampled rectangular fields in a non-rotational symmetric system.

$$z(x, y) = \frac{c(x^2 + y^2)}{1 + \sqrt{1 - (1 + k)c^2(x^2 + y^2)}} + \sum_{i=0}^M C_i x^m y^n, \quad (2)$$

$$j = \frac{(m + n)^2 + m + 3n}{2} + 1,$$

where c is the vertex curvature, k is the conic constant, and C_i is the coefficient of polynomial $x^m y^n$ ($m \geq 0, n \geq 0$). Owing to the symmetry about the XOZ and YOZ planes, the coefficients of the odd terms of x and y in Eq. (2) are zeros. It is worth pointing out that there does not exist a method for direct conversion to an xy -polynomial freeform surface from an aspherical surface, in particular, due to the even aspherical coefficients being up to the 10th order. A fitting algorithm could be implemented. However, high precision is advocated to minimize the deviation before and after conversion. In the design conception described here, the aspheric type is converted to the xy type through a mathematical scheme aiming to avoid significant deviation produced by the xy -polynomial freeform surface type. The aspheric type can be expressed as

$$z(r) = \frac{cr^2}{1 + \sqrt{1 - (1 + k)c^2r^2}} + Ar^4 + Br^6 + \dots + Ir^{20}, \quad (3)$$

where z is sag; k is the conic constant; c is the curvature of the refracting surface; $r = \sqrt{x^2 + y^2}$ is the height above the optical axis; and A, B, \dots, I are the coefficients of the even aspheric equation. It is essential to interpret the relationship between an even polynomial and a monomial polynomial to convert the even aspheric equation to a monomial equation. Considering the binomial distribution formula, the height of the optical surface can be expressed using Pascal's triangle, as given in Eq. (4):

$$r^{2n} = (x^2 + y^2)^n = C_0 x^{2*n} y^{2*0} + C_1 x^{2*(n-1)} y^{2*1} + \dots + C_{n-1} x^{2*1} y^{2*(n-1)} + C_n x^{2*0} y^{2*n}, \quad (4)$$

where $n = 2, 3, \dots, 10$. The numbers of $C_0, C_1, \dots, C_{n-1}, C_n$ are from the $(n+1)$ st row of Pascal's triangle.

Combining Eq. (3) with Eq. (4), each term is a polynomial in the expansion of $(x^2 + y^2)^n$. Compared with Eq. (2), the coefficients of the xy polynomial can be obtained. By doing so, the even aspheric surface can be converted to an xy -polynomial surface more easily without sacrificing optical performance.

(6) Analysis of system performance.

3. STARTING POINT SELECTION AND PERFORMANCE EVALUATION

In this section, the development of a wide-angle camera design using all-aspherical surfaces and a compact architecture optimized with aspheric surfaces in combination with freeform surfaces will be discussed and demonstrated.

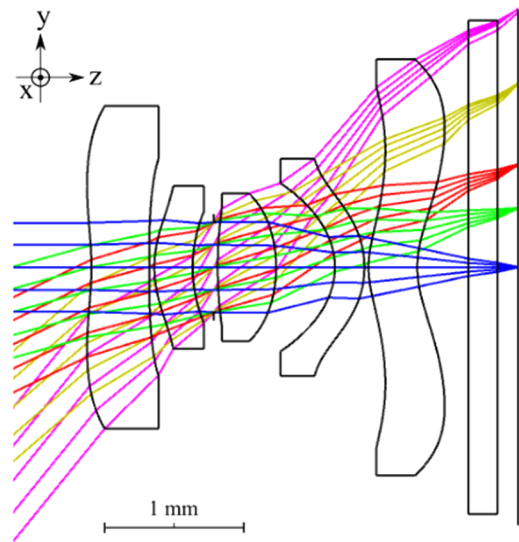


Fig. 2. Optical layout of the starting point.

A. Starting Point Selection for Optimization

Selecting a potential starting point for the design is very critical as it reduces the dependence on advanced design skills considerably. Based on the requirements of the physical constraint to form a slim structure and stringent design requirements of a large FoV, high resolution, and low f -number, a 5P construction was selected as a starting point. The starting point is a mobile-based camera lens of 103° full FoV, 3.62 mm TTL, and $f/2.4$ [18]. The goal is to maintain the exact same main characteristics (FoV and f -number) while increasing the footprint, ensuring the miniaturization and improvement of optical performance. The established starting point, as shown in Fig. 2, has five aspherical optical elements, with the first and fifth elements concave close to the axis and convex off-axis, the second and fourth elements with negative power, and the third element with positive optical power. The aperture stop is located between

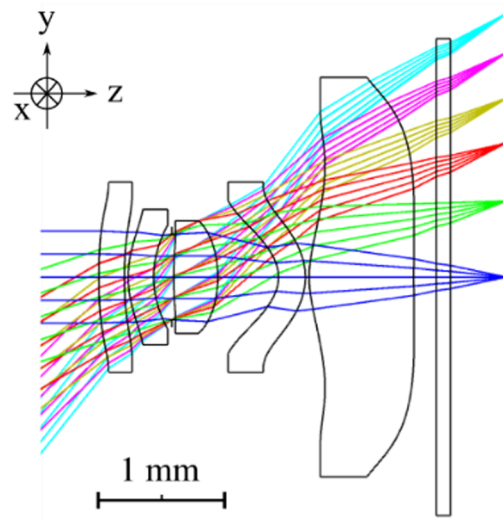


Fig. 3. Layout of the wide-angle camera lens benchmark design with all-aspherical surfaces.

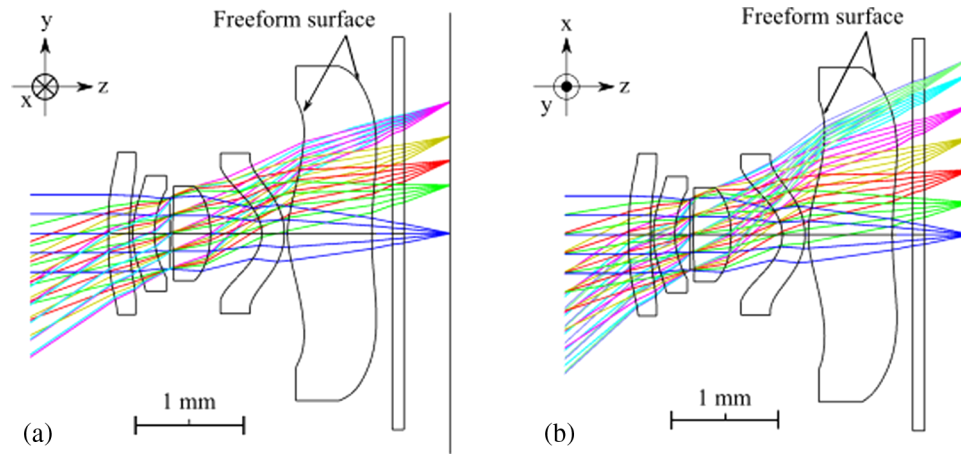


Fig. 4. Layout of freeform design of the optical ray paths along (a) YOZ and (b) XOZ planes.

Table 1. Target Design Specifications and Sensor Parameters for All-Aspherical Design and Freeform Design

Target Design Specifications		Main Parameters of the Selected Sensor	
Parameters	Values	Parameters	Values
TTL	3.19 mm	Sensor size	1/4.4"
Diagonal FoV	103°	Active area of sensor	3322.37 $\mu\text{m} \times$ 2499.84 μm
F -number	2.4	Resolution	3264 \times 2448 (pixels)
Back focal length	≥ 0.6 mm	Pixel size	1.008 μm

the second and third lenses, which satisfies the most beneficial conditions for low distortion of the wide-angle camera lens.

B. All-Aspherical Design versus Freeform Design

To fully explore the superiority of freeform optics over aspherical surfaces, it is necessary to design the wide-angle lens with only aspherical surfaces. The optimization of the starting point is conducted in Zemax-OpticsStudio design software. The final version of the new architecture with only aspherical surfaces is shown in Fig. 3. The surface profile for the first surface of the first element is converted to concave from an S-shaped profile to ensure the wide-angle feature of the wide-angle camera lens. As is well known, transverse reduces as the number of aspheric coefficients increase. Thus, the even aspheric surface with 20th order terms at the last element was considered. Table 1 summarizes the target design specifications and the main parameters of the sensor for the system.

The all-aspherical design will be used as a benchmark comparison for the purpose of emphasizing the variation between this and the freeform design. The next step of the adjustment for all-aspherical design is the combination of the freeform surface. Therefore, it is essential to select a suitable freeform surface for the wide-angle camera lens. We chose the last element as the freeform element because the proximity of the image plane helps to keep other aberrations in check after the freeform surfaces are applied. Therefore, the second surface of the fifth element

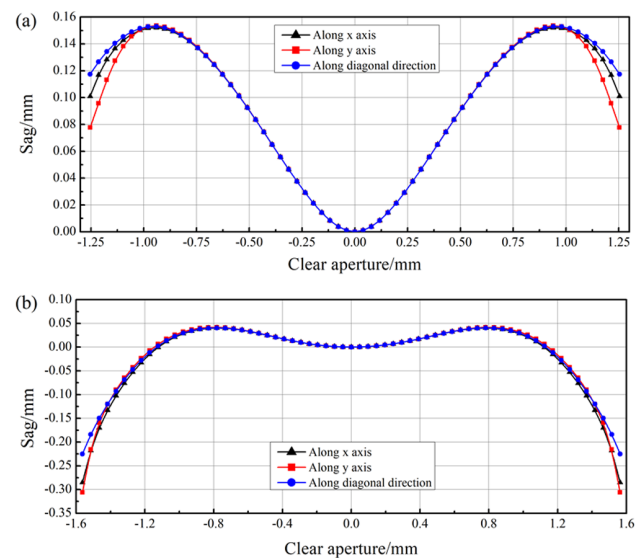


Fig. 5. Freeform surface profile along different directions. (a) First surface of the fifth element and (b) second surface of the fifth element in Fig. 4.

is converted to xy -polynomial type from the even aspheric surface, and asymmetric coefficients up to the 230th order are used as variables. It is important to remark that this value corresponds to the 20th order term of the even aspheric surface. To further improve the image quality to a high level to reach acceptance criteria, we also convert the aspheric-type surface to the xy -type surface at the first surface of the fifth element. Use of freeform surfaces in succession allows better system performances and specifications to be realized, and also allows optical systems with low cost to be offered. The architecture of the final freeform design is shown in Fig. 4. The cross-sectional profiles of the freeform lens are shown in Fig. 5. As demonstrated in this figure, the freeform surface profiles are not clearly distinguished in the central region, but deviation of the surface profiles occurs on the peripheral field. In terms of optics manufacturing and testing, the manufacturability and cost are the main concerns for designers during the design process. To reduce the cost and

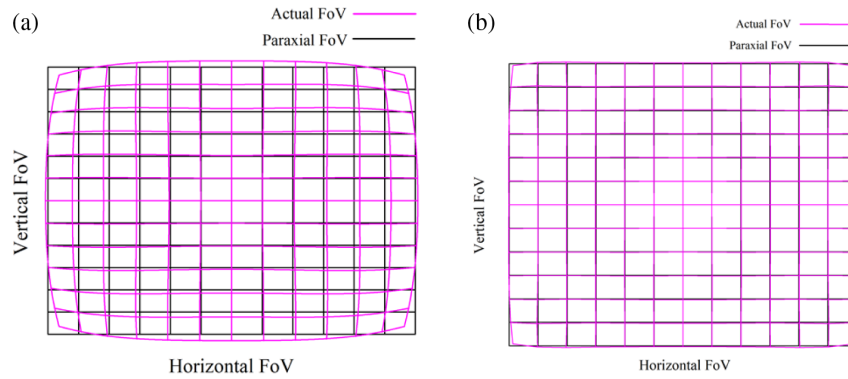


Fig. 6. Distortion grid of (a) all-aspherical design and (b) freeform design.

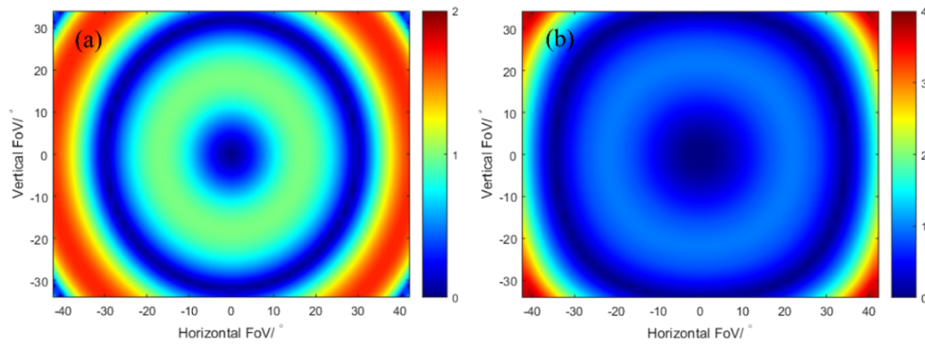


Fig. 7. 2D lateral color field maps of the (a) all-aspherical design and (b) freeform design.

difficulty in manufacturing and assembling, only two freeform surfaces are utilized in this design example.

One of the most promising techniques of freeform optics is its capability to correct distortion compared to non-freeform designs. The standard for mobile imaging architecture TV (SMIA-TV) distortion is used to assess image deformation, which is given by [19]

$$\text{SMIA TV distortion (\%)} = \frac{h' - h}{h'} \times 100, \quad (5)$$

where h stands for half-height in the center, and h' represents half-height in the image corner. The optical distortion for all-aspherical design is given in Fig. 6(a). TV distortion is about 6.7%. Distortion for the freeform design has been corrected to be less than 2%, as illustrated in Fig. 6(b). Distortion can be negligible or easily corrected using image processing. Therefore, the design using aspherical surfaces combining freeform surfaces could greatly decrease distortion.

Current camera lenses require that the lateral color must be within two times the size of a pixel. A minor drawback of the optical design software is that it does not have 2D image quality analysis tools. Because optical design software has a built-in macro that extends standard program capabilities, we create our freeform diagnostic tools to facilitate system optimization. Following Eq. (6), the 2D lateral color is calculated by the absolute difference of the chief ray between maximum image height and minimum image height from the short wavelength to the long wavelength:

$$\Delta_\lambda = |(x_s - x_l)^2 + (y_s - y_l)^2|, \quad (6)$$

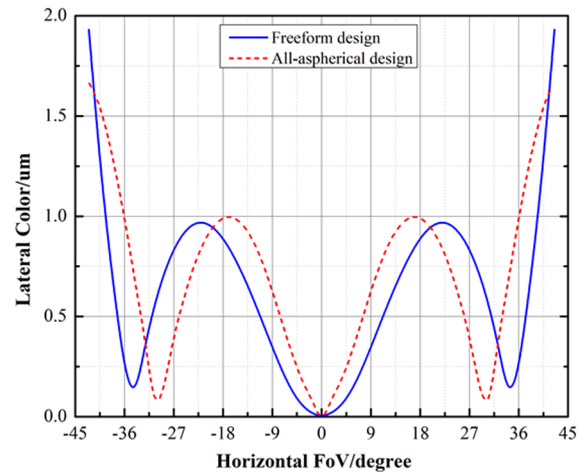


Fig. 8. Horizontal cross section through the 2D lateral color distribution along $y = 0^\circ$ in Fig. 7.

where (x_s, y_s) and (x_l, y_l) represent the locations of the chief rays of short and long wavelengths at the image plane, respectively. As shown in Fig. 7(a), the 2D lateral color field map for an all-aspherical design that demonstrates a rotationally symmetric design is far below $2 \mu\text{m}$. The maximum departure of $1.68 \mu\text{m}$ is located at 41° half-FoV. Figure 7(b) shows the 2D lateral color field map for freeform design. The field map has lost certain symmetry over the full FoV because of the on-symmetric optical system. The maximum departure of lateral color is $3.54 \mu\text{m}$, which is located in the corner field. The cross sections of lateral color distribution for $y = 0^\circ$ for the all-aspherical design and

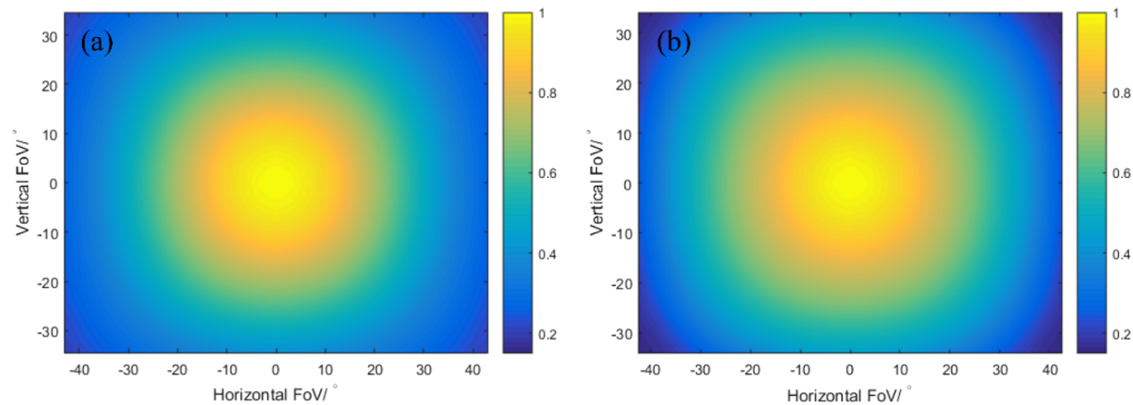


Fig. 9. Relative illumination distribution of the (a) all-aspherical design and (b) freeform design in image sensor.

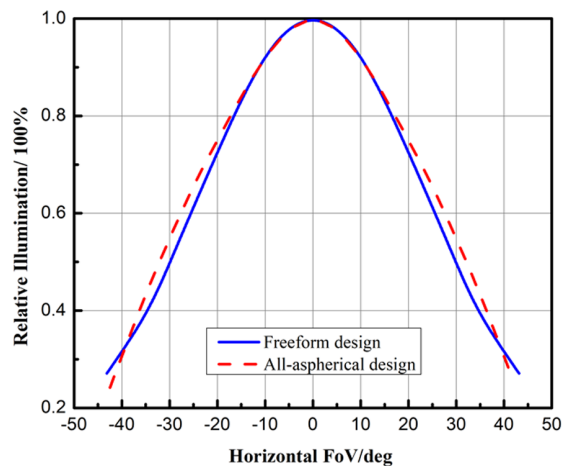


Fig. 10. RI as a function of horizontal FoV in Fig. 9.

freeform design are shown in Fig. 8. The results show that the lateral color from 0.0 field to 0.8 field is less than $2.0\ \mu\text{m}$. In comparison to the all-aspherical design, the distortion correction causes a slightly worse lateral color for freeform design; however, it is still at an acceptable value.

The 2D RI distributions for the all-aspherical design and freeform design are depicted in Fig. 9. It can be observed that the RI of the freeform design likewise shows symmetrical distribution. As shown in Fig. 9(b), the RI in the corner FoV is lower than the

RI of the all-aspherical design shown in Fig. 9(a). Figure 10 gives the RI along the $y = 0^\circ$. The RI value for all-aspherical design, represented by a red dashed line, is over 24.2%, while the RI value for freeform design, denoted by a blue solid line, is over 27.1%. Therefore, distortion correction comes with the penalty of decreased RI in the case of the freeform design.

To evaluate the superposition of primary and third-order aberrations, the root mean square (RMS) spot radius with respect to the chief ray is used as a criterion for assessing the image quality over the full FoV. 2D RMS spot radius field maps are shown in Fig. 11. As we can see in Fig. 11(a), the RMS spot radius of the all-aspherical design is considerably small, while the maximum field has an RMS spot radius of $1.63\ \mu\text{m}$. In the case of the freeform design shown in Fig. 11(b), the maximum spot radius appears in the corner field (about $2.32\ \mu\text{m}$). Also, the non-symmetrical distribution can be clearly observed.

The average modulation transfer function (MTF), which is given by the average value of sagittal and tangential values, is chosen to evaluate the overall image sharpness. As illustrated in Fig. 12, the average MTF is mapped across the full field at 120 lp/mm spatial frequency. In Fig. 12(b), the freeform design has an appearance non-symmetrical distribution of average MTF. The average MTF values along $y = 0^\circ$ in Fig. 12 are given in Fig. 13. As shown in this figure, there is a dramatic fall in terms of average MTF of the all-aspherical design because of the constraints of TTL that lead to a sharp decrease in tangential MTF. The MTF of the freeform design declines steadily, depicting that

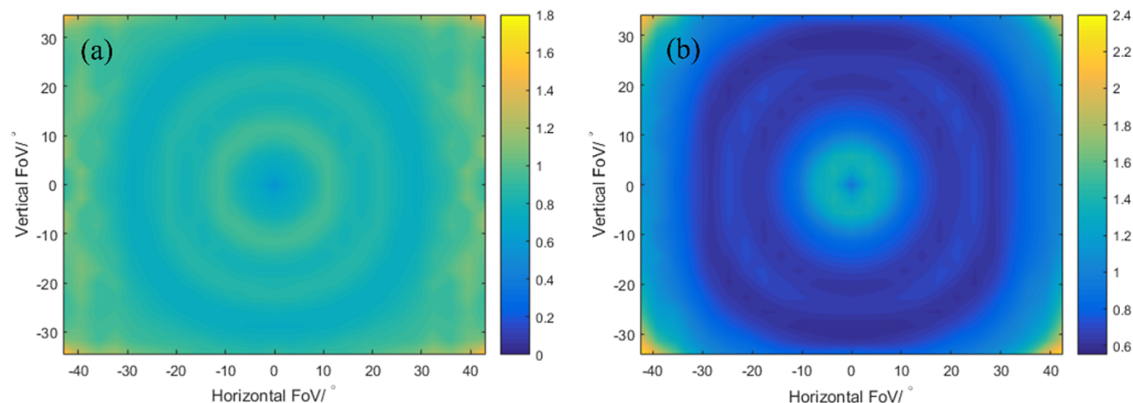


Fig. 11. 2D spot radius field maps for the (a) all-aspherical design and (b) freeform design.

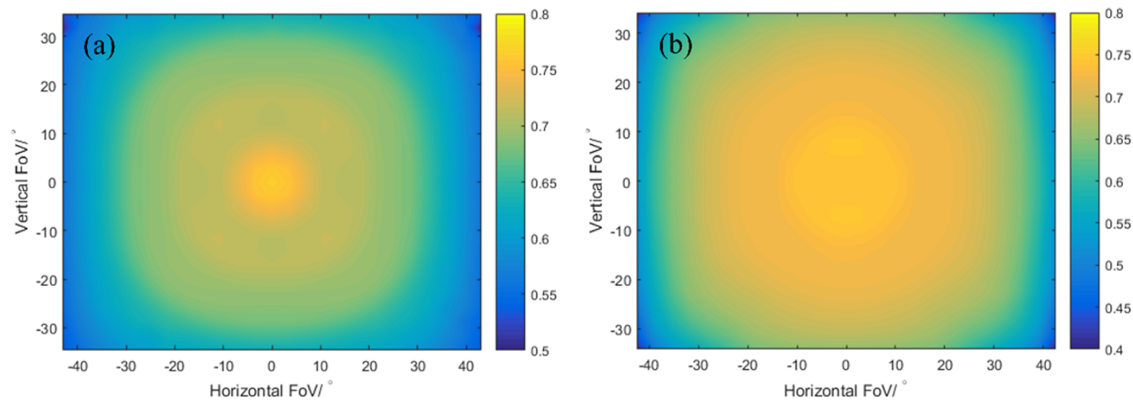


Fig. 12. Field maps of average MTF for (a) all-aspherical design and (b) freeform design.

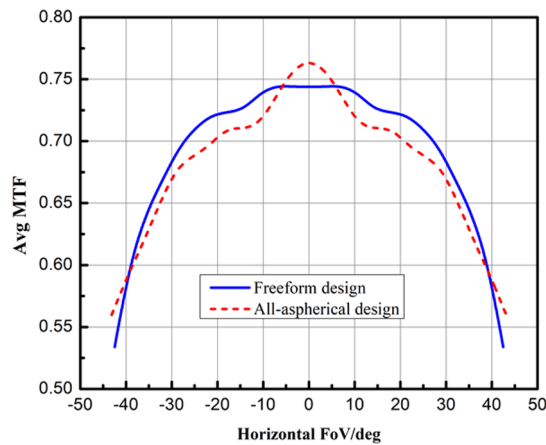


Fig. 13. Horizontal cross section through the average MTF distribution along $y = 0^\circ$ in Fig. 12.

freeform surfaces play a significant role in reducing the divergence between tangential MTF and sagittal MTF. However, the example of all-aspherical design shows better performance at the edge field. Therefore, distortion tends to reduce at the expense of MTF performance at the edge field in the case of freeform design.

To investigate the penalty of the as-built performance of both all-aspherical design and freeform design, a Monte Carlo sensitivity analysis is conducted. Both systems are individually perturbed with each tolerance. The tolerance values in Ref. [15] are used to conduct tolerance analysis. Because the non-rotational symmetric surface is applied in the freeform design, its tolerance analysis is more complex compared to the all-aspherical design. The alpha/beta/gamma tilt and x/y displacement of the freeform element of the freeform design are taken into account. We selected average diffraction MTF at 120 lp/mm as the performance metric. The back focal length is defined as a compensator, and 500 Monte Carlo runs were performed. Table 2 lists the analysis results of the probable average diffraction MTF with different cumulative probabilities. As shown in Table 2, the freeform design has higher MTF values than all-aspherical design. According to the tolerance errors, the sensitive tolerances are listed in order: fringe irregularity (namely, the fringes are formed from the comparison of the test surface to the reference surface) at the first surface of

Table 2. Cumulative Probability Obtained from Monte Carlo Simulation

	90%	80%	50%	20%	10%
All-aspherical design	0.418	0.459	0.523	0.568	0.585
Freeform design	0.441	0.487	0.552	0.594	0.612

Table 3. Comparison of Performance between All-Aspherical Design and Freeform Design

Items	All-Aspherical Design	Freeform Design
Number of aspheric surfaces	10	8
Number of freeform surfaces	0	2
Effective focal length	1.74 mm	1.80 mm
TTL	3.19 mm	3.19 mm
F -number	2.43	2.44
Diagonal FoV	102.7°	109°
TV distortion	−5.7%	−1.9%
Lateral color		
0.7 field	0.66 μm	0.90 μm
1.0 field	1.52 μm	3.54 μm
RI		
0.7 field	34.9%	38.2%
1.0 field	20%	16%
Tangential MTF		
0.7 field	44.4%	52.4%
1.0 field	31.5%	20.2%
Sagittal MTF at		
0.7 field	68%	72.8%
1.0 field	64.4%	45.6%

lens 3, thickness at lens 4, and surface decenter at the first surface of lens 2. It is apparent that the freeform element is insensitive in terms of tilt and decenter tolerances.

C. Comparison

It is necessary to understand whether using even aspheric surfaces combining freeform surfaces will help enhance performance. For the purpose of highlighting differences, a quantitative comparison of both design cases utilizing all even aspheric surfaces and aspheric surfaces in combination with freeform surfaces are summarized in Table 3. The freeform design demonstrated the ability of correcting distortion and obtaining a larger FoV. Moreover, the freeform design can also offer higher RI and MTF in the 0.7 field, while the freeform design presented does not appreciably increase the lateral color

in the 0.7 field. Results show, however, that the freeform design also experiences further deterioration in terms of lateral color, RI, and MTF at the peripheral field. We can thus conclude that distortion, RI, lateral color, and MTF are mutually restricted parameters. The benefit of having freeform surfaces is significant and noticeable. However, it cannot appreciably improve the specified performance without a penalty on other performances; for example, the cost and complexity of manufacturing freeform lenses as well as alignment are greatly intensified.

4. CONCLUSION

In this work, we presented a wide-angle camera lens with less distortion by employing the combination of even aspheric surfaces and freeform surfaces. A freeform surface description to optimally design a wide-angle camera lens was detailed, and then a more accurate aspherical/freeform surface conversion scheme was introduced. We verified the effectiveness of the proposed method and developed freeform diagnostic tools. Compared with traditional wide-angle camera lens design using even aspheric surfaces, where it is challenging to correct distortion, freeform surfaces offer a noticeable benefit in distortion correction over a rectangular field, and without rotational symmetry of the field, it is more efficient to correct distortion by breaking the rotational symmetry of the last two optical surfaces. One cannot gain much from using freeform surfaces in centered lens design with a rotationally symmetric circular field. We provide deeper insight in image quality in the case of a non-rotationally symmetric system. We strongly believe that the research content presented here could promote utilization of freeform surfaces in wide-angle camera lenses and provide some references for other freeform techniques and optimum design of freeform optics.

Disclosures. The authors declare no conflicts of interest.

Data availability. Data underlying the results presented in this paper are not publicly available at this time but may be obtained from the authors upon reasonable request.

REFERENCES

1. D. G. Bailey, "A new approach to lens distortion correction," in *Proceedings Image and Vision Computing New Zealand* (2002), pp. 59–64.
2. C. Ricolfe-Viala, A. J. Sanchez-Salmeron, and A. Valera, "Efficient lens distortion correction for decoupling in calibration of wide angle lens camera," *IEEE Sens. J.* **13**, 854–863 (2012).
3. K. H. Choi and C. Kim, "Proposed new AV-type test-bed for accurate and reliable fish-eye lens camera self-calibration," *Sensors* **21**, 2776 (2021).
4. K. T. Gribbon, C. T. Johnston, and D. G. Bailey, "A real-time FPGA implementation of a barrel distortion correction algorithm with bilinear interpolation," in *Image and Vision Computing New Zealand* (2003), pp. 408–413.
5. S. Chang, D. Kim, and H. S. Kwon, "Compact wide-angle capsule endoscopic lens design," *Appl. Opt.* **59**, 3595–3600 (2020).
6. M. J. Sheu, C. W. Chiang, W. S. Sun, J. J. Wang, and J. W. Pan, "Dual view capsule endoscopic lens design," *Opt. Express* **23**, 8565–8575 (2015).
7. J. Hou, H. F. Li, R. M. Wu, P. Liu, Z. R. Zheng, and X. Liu, "Method to design two aspheric surfaces for imaging system," *Appl. Opt.* **52**, 2294–2299 (2013).
8. Y. F. Nie, D. R. Shafer, H. Ottevaere, H. Thienpont, and F. Duerr, "Freeform imaging system design with multiple reflection surfaces," *Proc. SPIE* **11895**, 75–88 (2021).
9. F. Duerr and H. Thienpont, "Freeform imaging systems: Fermat's principle unlocks 'first time right' design," *Light Sci. Appl.* **10**, 95 (2021).
10. Z. F. Zhuang, Y. T. Chen, F. H. Yu, and X. W. Sun, "Field curvature correction method for ultrashort throw ratio projection optics design using an odd polynomial mirror surface," *Appl. Opt.* **53**, E69–E76 (2014).
11. Y. X. Bian, H. F. Li, Y. F. Wang, Z. R. Zheng, and X. Liu, "Method to design two aspheric surfaces for a wide field of view imaging system with low distortion," *Appl. Opt.* **54**, 8241–8247 (2015).
12. Y. F. Nie, R. Mohedane, P. Benítez, J. Chaves, J. C. Miñano, H. Thienpont, and F. Duerr, "Multifield direct design method for ultrashort throw ratio projection optics with two tailored mirrors," *Appl. Opt.* **55**, 3794–3800 (2016).
13. J. Sasián, D. Reshidko, and C. L. Li, "Aspheric/freeform optical surface description for controlling illumination from point-like light sources," *Opt. Eng.* **55**, 115104 (2016).
14. Y. F. Yan and J. Sasián, "Miniature camera lens design with a freeform surface," *Proc. SPIE* **10590**, 1059012 (2017).
15. Z. F. Zhuang, X. Dallaire, J. Parent, P. Roulet, and S. Thibault, "Geometrical-based quasi-aspheric surface description and design method for miniature, low-distortion, wide-angle camera lens," *Appl. Opt.* **59**, 8408–8417 (2020).
16. J. F. Ye, L. Chen, X. H. Li, Q. Yuan, and Z. S. Gao, "Review of optical freeform surface representation technique and its application," *Opt. Eng.* **56**, 110901 (2017).
17. C. Hou, Y. Ren, Y. Tan, Q. Xin, and Y. Zang, "Compact optical zoom camera module based on Alvarez elements," *Opt. Eng.* **59**, 025104 (2019).
18. F. J. Dai, "Wide-angle imaging lens," U.S. patent 10036875B2 (July 31, 2018).
19. R. L. Nicol, "Image sensor characterization using SMIA standard," *Proc. SPIE* **6196**, 130–141 (2006).